

# Superluminal $\gamma$ -rays from the Crab pulsar

Roman Tomaschitz \*

*Department of Physics, Hiroshima University, 1-3-1 Kagami-yama, Higashi-Hiroshima 739-8526, Japan*

Received 21 February 2006; received in revised form 8 August 2006; accepted 12 September 2006

Available online 5 October 2006

## Abstract

A tachyonic spectral fit to the pulsed  $\gamma$ -ray flux of the Crab is performed, based on the superluminal spectral densities generated by ultra-relativistic electrons. The  $\gamma$ -ray wideband of the pulsar can be reproduced by a tachyonic cascade spectrum, capable of generating the spectral curvature in double-logarithmic plots as well as the extended spectral plateau defined by COMPTEL and EGRET flux points in the MeV band. Estimates on the magnetospheric electron population generating the radiation are inferred from the spectral fit, such as power-law indices, electron temperature and the electronic source count.

© 2006 Elsevier B.V. All rights reserved.

*PACS:* 95.30.Gv; 11.10.Lm; 97.60.Gb; 98.70.Sa

*Keywords:* Superluminal cascade spectra; Tachyonic  $\gamma$ -rays; Longitudinal polarization; PSR B0531+21

## 1. Introduction

The goal is to point out evidence for the  $\gamma$ -ray spectrum of the Crab pulsar to be tachyonic. The most pronounced difference between electromagnetic and tachyonic radiation lies in the emission process. Due to the negative mass-square of the radiation field, there is a residual radiation that persists in the limit of large orbital bending radius, so that freely moving electrons can radiate superluminal quanta. Radiation densities attached to uniformly moving charges have no analog in electrodynamics, their very existence has substantial implications for the spacetime structure, requiring an absorber medium [1–3]. The Green function of the superluminal radiation process is time-symmetric, there is no retarded propagator supported outside the lightcone. The advanced modes of the radiation field are converted into retarded ones by virtue of a nonlocal, instantaneous interaction with the absorber. The latter defines a universal frame of reference, necessary to render

the superluminal signal transfer causal. The time symmetry of the Green function implies that there is no radiation damping, the radiating charge stays in uniform motion, the energy radiated is supplied by the oscillators constituting the absorber medium. The superluminal spectral densities depend on the velocity of the charge in the rest frame of the absorber. I also mention that tachyons and photons couple only indirectly via matter fields, there is no absorption of high-energy tachyons by the infrared background. At  $\gamma$ -ray energies, the speed of tachyons is very close to the speed of light, the noticeable difference to electromagnetic radiation is the longitudinally polarized flux component. The polarization of tachyons can be determined from transversal and longitudinal ionization cross-sections, which peak at different scattering angles.

These features of tachyonic wave propagation have been elaborated in previous papers, here we focus on a specific example, a tachyonic spectral fit to the pulsed  $\gamma$ -ray flux of the Crab. When tachyonic spectral densities are averaged with thermal or power-law electron densities, this leads to cascade spectra, extended spectral plateaus followed by power-law decay terminating in exponential decay. A glance at the  $\gamma$ -ray broadband of the Crab pulsar suggests

\* Tel.: +81 824 247361; fax: +81 824 240717.

*E-mail address:* [roman@geminga.org](mailto:roman@geminga.org)

that it can readily be fitted by a cascade spectrum, cf. the figures in Section 3.

In Section 2, we explain the transversal and longitudinal spectral densities of uniformly moving charges, as well as their averaging with thermal and exponentially cut power-law electron distributions. The spectral averaging can be done in closed form, and high- and low-temperature expansions of the tachyonic spectral densities are derived. The spectral breaks and slopes of tachyonic cascade spectra are discussed. In Section 3, we perform the spectral fit to the pulsed Crab  $\gamma$ -wideband, infer the cutoff temperature of the electronic/protonic source populations, and compare it to the break energies in the cosmic-ray spectrum. In Section 4, we present our conclusions.

## 2. Superluminal spectral densities and spectral averages

The transversal and longitudinal tachyonic radiation densities of a uniformly moving electron read [3]

$$p^{\text{T,L}}(\omega, \gamma) = \frac{\alpha_q m_t \omega}{\omega^2 + m_t^2} \left[ \gamma^2 - \left( 1 + \frac{\omega^2}{m_t^2} \right) \Delta^{\text{T,L}} \right] \frac{1}{\gamma \sqrt{\gamma^2 - 1}}, \quad (1)$$

where  $\Delta^{\text{T}} = 1$  and  $\Delta^{\text{L}} = 0$ .  $\gamma$  is the electronic Lorentz factor,  $\alpha_q$  the tachyonic fine structure constant, and  $m_t$  the tachyon mass. The spectral cutoff occurs at  $\omega_{\text{max}}(\gamma) := m_t \sqrt{\gamma^2 - 1}$ . Only frequencies in the range  $0 < \omega < \omega_{\text{max}}(\gamma)$  can be radiated by a uniformly moving charge, the tachyonic spectral densities  $p^{\text{T,L}}(\omega)$  are cut off at the break frequency  $\omega_{\text{max}}$ . The units  $\hbar = c = 1$  can easily be restored. We use the Heaviside–Lorentz system, so that  $\alpha_q = q^2/(4\pi\hbar c) \approx 1.0 \times 10^{-13}$ . The tachyon mass is  $m_t \approx 2.15 \text{ keV}/c^2$ , the tachyon–electron mass ratio  $m_t/m \approx 1/238$ . These estimates are obtained from hydrogenic Lamb shifts [4]. The tachyonic count rates (tachyons emitted per unit time and unit frequency interval) are  $n^{\text{T,L}}(\omega) := p^{\text{T,L}}(\omega)/\omega$ .

The radiation densities (1) refer to a single charge with Lorentz factor  $\gamma$ . We average them with electron distributions, power-laws exponentially cut with Boltzmann densities,  $d\rho \propto E^{-2-\alpha} e^{-E/(kT)} d^3p$ , or

$$d\rho_{\alpha,\beta}(\gamma) := \gamma^{-\alpha-1} e^{-\beta\gamma} \sqrt{\gamma^2 - 1} d\gamma, \quad (2)$$

where  $\beta := mc^2/(kT)$ . At  $\alpha = -2$ , the distribution is thermal. The electronic Lorentz factors range in an interval  $\gamma_1 \leq \gamma < \infty$ . The normalization factors  $A_{\alpha,\beta}(\gamma_1, n_1)$  of densities (2) are determined by  $n_1 = A_{\alpha,\beta}(\gamma_1, n_1) \int_{\gamma_1}^{\infty} d\rho_{\alpha,\beta}(\gamma)$ , where  $n_1$  is the electron count and  $\gamma_1$  the smallest Lorentz factor of the source population.

The averaging is carried out via

$$\langle p^{\text{T,L}}(\omega; \gamma_1, n_1) \rangle_{\alpha,\beta} := A_{\alpha,\beta}(\gamma_1, n_1) \int_{\gamma_1}^{\infty} p^{\text{T,L}}(\omega, \gamma) \times \theta(\omega_{\text{max}}(\gamma) - \omega) d\rho_{\alpha,\beta}(\gamma), \quad (3)$$

with  $\omega_{\text{max}}(\gamma)$  defined above. These averages can be reduced to the spectral functions

$$\begin{aligned} B^{\text{T,L}}(\omega; \gamma; \alpha, \beta) &:= \int_{\gamma}^{\infty} p^{\text{T,L}}(\omega, \tilde{\gamma}) d\rho_{\alpha,\beta}(\tilde{\gamma}) \\ &= \frac{\alpha_q m_t \hat{\omega}}{1 + \hat{\omega}^2} \frac{1}{\gamma^{\alpha+1} \beta^2} \left\{ [(1 + \alpha)\alpha \right. \\ &\quad \left. - \beta^2(1 + \hat{\omega}^2) \Delta^{\text{T,L}}](\beta\gamma)^{\alpha+1} \Gamma(-\alpha - 1, \beta\gamma) \right. \\ &\quad \left. - (\alpha - \beta\gamma) e^{-\beta\gamma} \right\}, \end{aligned} \quad (4)$$

where  $\hat{\omega} := \omega/m_t$  and  $\Delta^{\text{T,L}}$  as in (1).

The spectral range of the radiation densities (1) is  $0 < \omega < \omega_{\text{max}}(\gamma)$ . Inversely, the condition  $\omega_{\text{max}}(\hat{\gamma}) - \omega = 0$  or  $\hat{\gamma}(\omega) := \sqrt{1 + \hat{\omega}^2}$  defines the minimal electronic Lorentz factor for radiation at this frequency. ( $\hat{\omega}$  stands for the rescaled frequency  $\omega/m_t$ .) That is, an electron in uniform motion can radiate at  $\omega$  only if its Lorentz factor exceeds  $\hat{\gamma}(\omega)$ . The lower edge of Lorentz factors in the electronic source distribution defines the break frequency,  $\omega_1 := \omega_{\text{max}}(\gamma_1)$ , or  $\omega_1/m_t = \sqrt{\gamma_1^2 - 1}$ , which separates the spectrum into a low- and high-frequency band. We have  $\hat{\gamma}(\omega_1) = \gamma_1$ , and  $\hat{\gamma}(\omega) > \gamma_1$  if  $\omega > \omega_1$ . The averaged energy density (3) can thus be assembled as

$$\begin{aligned} \langle p^{\text{T,L}}(\omega; \gamma_1, n_1) \rangle_{\alpha,\beta} &= A_{\alpha,\beta}(\gamma_1, n_1) [B^{\text{T,L}}(\omega; \gamma_1; \alpha, \beta) \theta(\omega_1 - \omega) \\ &\quad + B^{\text{T,L}}(\omega; \hat{\gamma}(\omega); \alpha, \beta) \theta(\omega - \omega_1)]. \end{aligned} \quad (5)$$

The superscripts T and L denote the transversal and longitudinal polarization components. If the polarization is not distinguished, we add the polarization components, writing  $\langle p^{\text{T+L}} \rangle_{\alpha,\beta}$  for the unpolarized density.

To obtain the low-temperature expansion,  $\beta \gg 1$ , of the spectral average (5), we substitute the asymptotic expansion of the incomplete  $\Gamma$ -function [5] into the spectral function  $B^{\text{T,L}}(\omega; \gamma; \alpha, \beta)$ ,

$$\begin{aligned} B^{\text{T,L}}(\omega; \gamma; \alpha, \beta) &\sim \frac{\alpha_q m_t \hat{\omega}}{1 + \hat{\omega}^2} \frac{e^{-\beta\gamma}}{\gamma^\alpha \beta} \left[ C_0^{\text{T,L}}(\gamma) + \frac{C_1^{\text{T,L}}(\gamma)}{\beta\gamma} + \dots \right], \\ C_0^{\text{T,L}}(\gamma) &:= 1 - \Delta^{\text{T,L}} \frac{1 + \hat{\omega}^2}{\gamma^2}, \\ C_1^{\text{T,L}}(\gamma) &:= -\alpha + (2 + \alpha) \Delta^{\text{T,L}} \frac{1 + \hat{\omega}^2}{\gamma^2}. \end{aligned} \quad (6)$$

The expansion parameter is  $\beta\gamma \gg 1$ . The high-temperature expansion,  $\beta \ll 1$ , of  $B^{\text{T,L}}$  in (4) is based on the ascending series of  $\Gamma(-\alpha - 1, \beta\gamma)$ ,

$$\begin{aligned} B^{\text{T,L}}(\omega; \gamma; \alpha, \beta) &= \frac{\alpha_q m_t \hat{\omega}}{1 + \hat{\omega}^2} \gamma^{1-\alpha} \left( \left[ (1 + \alpha)\alpha - (\beta\gamma)^2 \Delta^{\text{T,L}} \frac{1 + \hat{\omega}^2}{\gamma^2} \right] \right. \\ &\quad \times \Gamma(-\alpha - 1) (\beta\gamma)^{\alpha-1} + D_0^{\text{T,L}} - \beta\gamma D_1^{\text{T,L}} \\ &\quad \left. + \frac{(\beta\gamma)^2}{2!} D_2^{\text{T,L}} - \dots \right), \\ D_k^{\text{T,L}}(\hat{\omega}; \gamma, \alpha) &:= \frac{1}{\alpha - k - 1} - \frac{\Delta^{\text{T,L}}}{\alpha - k + 1} \frac{1 + \hat{\omega}^2}{\gamma^2}, \end{aligned} \quad (7)$$

which requires  $\beta\gamma \ll 1$ . In the opposite limit,  $\beta\gamma \gg 1$ , we may still use the low-temperature expansion (6), even if  $\beta \ll 1$ . Singularities occurring at integer  $\alpha$  in (7) cancel if  $\varepsilon$ -expanded.

If  $\gamma_1 = 1$ ,  $\beta \ll 1$  and  $\alpha > 1$ , the maximum of  $\langle p^{T,L}(\omega; \gamma_1, n_1) \rangle_{\alpha, \beta}$ , cf. (5), is determined by the lead factor  $\propto \omega \hat{\gamma}^{-\alpha-1}$  in the high-temperature expansion (7). This peak is located at  $\omega_{\max} \approx m_t/\sqrt{\alpha}$  and is followed by power-law decay  $\propto \omega^{-\alpha}$  for  $\omega \ll m_t/\beta$  and exponential decay starting at about  $\omega \approx m_t/\beta$ . The low-temperature expansion (6) applies for  $\omega \gg m_t/\beta$ . If  $\gamma_1 \gg 1$  (but still  $\beta\gamma_1 \ll 1$  and  $\alpha > 1$ ), the peak of  $\langle p^{T,L}(\omega; \gamma_1, n_1) \rangle_{\alpha, \beta}$  is determined by the factor  $\omega/(\omega^2 + m_t^2)$  in (7) and occurs at  $\omega_{\max} \approx m_t$ . It is followed by a broken power-law, at first  $\langle p^{T,L} \rangle_{\alpha, \beta} \propto 1/\omega$ , in the range  $1 \ll \omega/m_t \ll \gamma_1$ , and then  $\langle p^{T,L} \rangle_{\alpha, \beta} \propto \omega^{-\alpha}$  in the interval  $\gamma_1 \ll \omega/m_t \ll 1/\beta$ . At  $\omega \approx m_t/\beta$ , there is an exponential cutoff according to (6).

The spectral fit is performed with the  $E^2$ -rescaled flux density  $E^2 dN^{T,L}/dE$ , which relates to the energy density  $\langle p^{T,L} \rangle_{\alpha, \beta}$  in (5) as

$$E^2 \frac{dN^{T,L}(E; \alpha, \beta, \gamma_1, n_1)}{dE} = \frac{\omega}{4\pi d^2} \langle p^{T,L}(\omega; \gamma_1, n_1) \rangle_{\alpha, \beta}, \quad (8)$$

where  $d$  is the distance to the pulsar. The preceding scaling relations for  $\langle p^{T,L} \rangle_{\alpha, \beta}$  give a plateau value  $E^2 dN^{T,L}/dE \propto 1$  in the range  $1 \ll E/(m_t c^2) \ll \gamma_1$ , followed by power-law decay  $E^2 dN^{T,L}/dE \propto E^{1-\alpha}$  in the band  $\gamma_1 \ll E/(m_t c^2) \ll 1/\beta$ , and subsequent exponential decay.

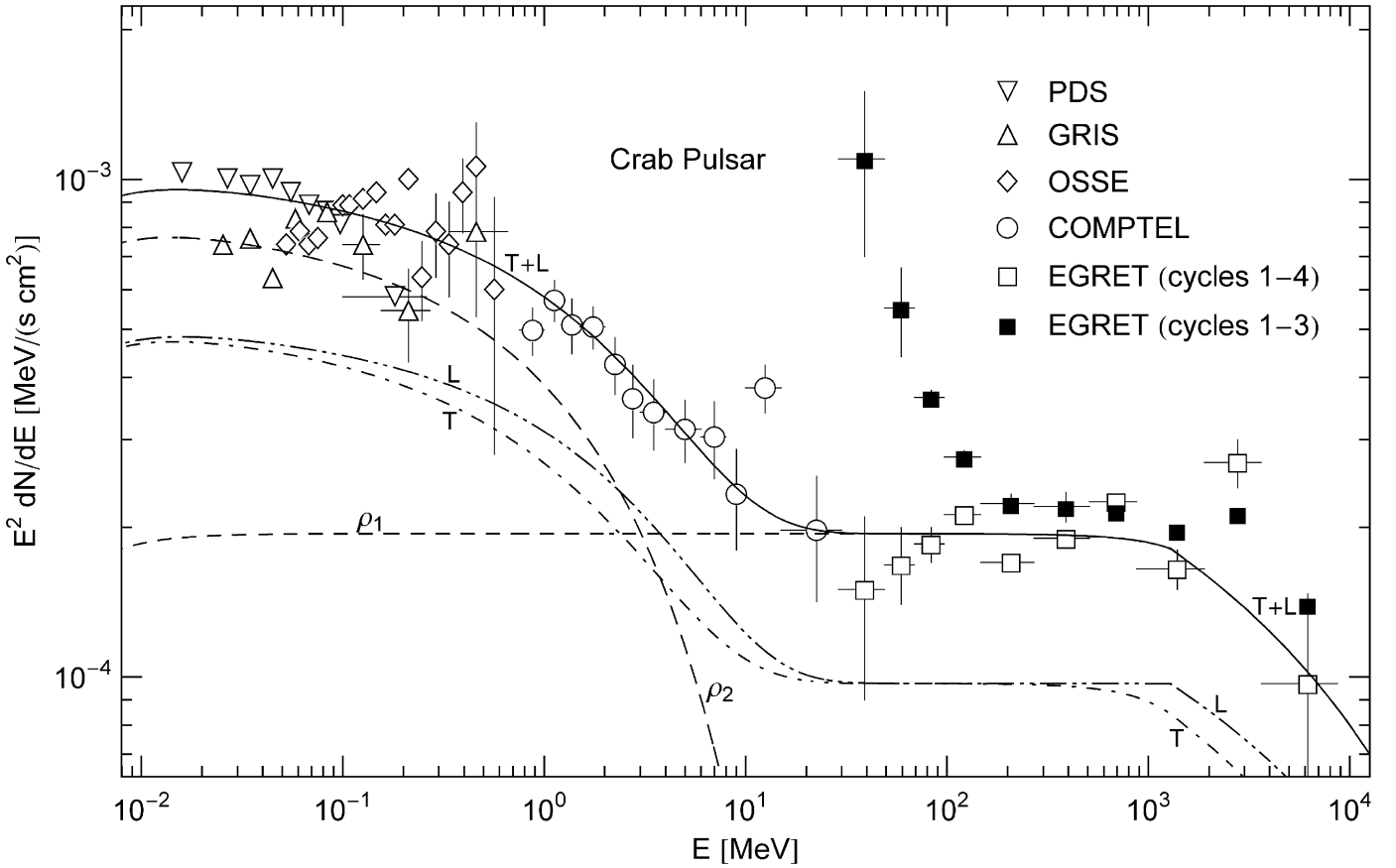


Fig. 1. Tachyonic spectral map of the Crab pulsar. PDS, COMPTEL and EGRET (open squares) data points from [7], GRIS points from [8], OSSE points from [9]; also see [10–12] for COMPTEL data on the pulsed Crab emission. The open squares are the final EGRET data covering cycles 1–4, corrected for spark chamber gas aging [13]. For comparison, we also indicate the EGRET flux points based on cycles 1–3, cf. [14]; the error bars on the last four flux points are suppressed, they are similar to those on the open squares with the same abscissa. In the  $\chi^2$ -fit, only the final EGRET data (open squares) are considered, and the vertical error bar on the second flux point is assumed to hold for the subsequent six points as well. The solid line T + L is the unpolarized differential tachyon flux  $dN^{T+L}/dE$ , rescaled with  $E^2$  for better visibility, cf. (12). The total flux T + L can be split into transversal (T, dot-dashed) and longitudinal (L, dot-dot-dashed) flux components  $dN^{T,L}/dE$ , cf. (13). The cascade spectra labeled  $\rho_{1,2}$  (dashed) are the unpolarized flux densities  $dN^{T+L}(E, \rho_i)/dE$  of two electron populations  $\rho_{i=1,2}$ , cf. Table 1 and (14). These cascades add up to the total flux T + L, which is the actual spectral fit with parameters (of the electron densities  $\rho_{i=1,2}$ ) listed in Table 1. The MeV plateau terminates in a nearly straight GeV power-law slope. In contrast to the  $\rho_2$ -cascade, the cutoff temperature of  $\rho_1$  is too high to significantly curve the power-law slope in the energy range covered here, cf. Fig. 3 for the wideband view. A spectral break at  $E \approx m_t \gamma_1 \approx 1.3$  GeV is visible as edge in the longitudinal spectral map, cf. after (8).  $\rho_1$  is the cascade producing the MeV plateau and the adjacent GeV power-law slope  $\propto 1/E$  ( $\alpha = 1$ , cf. Table 1). The soft  $\gamma$ -ray band is generated by adding the flux of the  $\rho_2$ -cascade to the  $\rho_1$ -plateau. The spectral curvature is caused by the Boltzmann factor in the averaged spectral densities, whose cutoff frequency is  $E_{\text{cut}} = (m_t/m)kT$ , defined by  $\hat{\gamma}(\omega_{\text{cut}}) = 1/\beta$  according to the low-temperature/high-frequency expansion (6). This implies cutoffs at 88 GeV for the  $\rho_1$ -cascade and 6.3 MeV for  $\rho_2$ . The cutoff temperature of the respective electron densities is recorded in Table 1. This figure is a close-up of the  $\gamma$ -wideband in Fig. 3.

In the foregoing discussion of the high-temperature asymptotics, we assumed an electron index  $\alpha > 1$ . We still have to settle the case  $\alpha < 1$ . The spectral peak at  $\omega_{\max} \approx m_t$  is again determined by the factor  $\omega/(\omega^2 + m_t^2)$ . Adjacent is a power-law slope  $\langle p^{T,L} \rangle_{\alpha,\beta} \propto 1/\omega$  in the range  $1 \ll \omega/m_t \ll 1/\beta$ , so that  $E^2 dN^{T,L}/dE \propto 1$ . At  $\omega \approx m_t/\beta$ , there is the cross-over to exponential decay, cf. (6). This holds true for  $\gamma_1 = 1$  as well as  $\gamma_1 \gg 1$ , provided  $\beta\gamma_1 \ll 1$ , since the leading order of the high-temperature expansion (7) does not depend on  $\gamma$  for  $\alpha < 1$ . If  $\beta\gamma_1 \gg 1$  despite of  $\beta$  being small, then the low-temperature expansion (6) applies instead of (7).

### 3. Tachyonic cascade spectra and spectral fits

Figs. 1–3 show the  $E^2$ -scaled differential number flux,  $E^2 dN^{T+L}/dE$ , as defined in (8), fitted to the data points. As the polarization is not observed, we add the transversal and longitudinal densities, writing  $\langle p^{T+L} \rangle := \langle p^T \rangle + \langle p^L \rangle$  for the energy density and  $dN^{T+L} := dN^T + dN^L$  for the number flux. We restore the natural units on the right-hand side of (8), up to now we have used  $\hbar = c = 1$ , and write  $E_{(1)}$  for  $\hbar\omega_{(1)}$ . The spectral maps are in MeV units, with the differential tachyon flux  $dN^{T,L}/dE$  in units of  $\text{MeV}^{-1} \text{s}^{-1} \text{cm}^{-2}$ . The normalization factor in (5) is dimensionless,  $A_{\alpha,\beta} = n_1 / \int_{\gamma_1}^{\infty} d\rho_{\alpha,\beta}(\gamma)$ , where  $n_1$  is the number of radiating electrons with Lorentz factors exceeding  $\gamma_1$ , distributed according to density (2).  $\alpha$  is the electronic power-law index, and  $\beta$  the exponential cutoff in the electron spectrum, both to be determined from the spectral fit like  $n_1$  and  $\gamma_1$ . As for the electron count  $n_1$ , it is convenient to use a rescaled parameter  $\hat{n}_1$  for the fit,

$$\hat{n}_1 := \frac{\alpha_q n_1}{\hbar[\text{keV s}] 4\pi d^2[\text{cm}]} \approx 1.27 \times 10^{-39} \frac{n_1}{d^2[\text{kpc}]}, \quad (9)$$

which determines the amplitude of the tachyon flux. Here,  $\hbar[\text{keV s}]$  implies the tachyon mass in keV units, that is, we put  $m_t c^2 \approx 2.15$  in the spectral function (4). The purpose of this rescaling is to avoid the distance estimate in the actual fitting procedure. Once  $\hat{n}_1$  is extracted from the spectral fit, we can calculate via (9) the number of radiating electrons  $n_1$  constituting the density  $d\rho_{\alpha,\beta}$ . This, however, implies that all tachyons reaching the detector are properly counted. At  $\gamma$ -ray energies, only a tiny  $\alpha_q/\alpha_e$ -fraction (the ratio of tachyonic and electric fine structure constant,  $\alpha_q/\alpha_e \approx 1.4 \times 10^{-11}$ ) of the tachyon flux is actually absorbed, cf. [6] and Section 4. This requires a rescaling of the electron count  $n_1$ , so that the actual number of radiating electrons is  $n_1^c := n_1 \alpha_e / \alpha_q \approx 7.3 \times 10^{10} n_1$ . In Table 1, we list the flux amplitude  $\hat{n}_1$  inferred from the spectral fit, as well as the renormalized electron count  $n_1^c$ . (In the table, we drop the subscript 1 in  $\hat{n}_1$  and  $n_1^c$ .) The density  $d\rho_{\alpha,\beta}$  is defined by parameters  $(\alpha, \beta, \gamma_1, \hat{n}_1 \rightarrow n_1 \rightarrow n_1^c)$  obtained from the spectral fit.

In the case of a thermal electron distribution ( $\alpha = -2$ ), we may identify  $kT [\text{TeV}] \approx 5.11 \times 10^{-7}/\beta$ . We use this def-

inition of electron temperature also for other electron indices  $\alpha$ .  $kT$  is the energy at which the exponential decay of the electron density (2) sets in. At high temperature, density (2) is peaked at  $\gamma_{\text{peak}} \approx -\alpha/\beta$ , provided  $\alpha < 0$  and  $\beta \ll |\alpha|$ ; the peak is followed by exponential decay. If  $\alpha > 0$ , the electron density is decreasing monotonically, at first as power-law and exponentially beyond  $kT$ . Nearly straight power-law slopes, as seen in the low GeV range of Fig. 1, can only emerge for electron indices  $\alpha > 1$ , cf. after (7). The spectral break from the MeV plateau into the power-law slope is determined by the lower edge  $\gamma_1$  of electronic Lorentz factors, cf. after (4). If  $\alpha < 1$ , the MeV plateau is followed by exponential decay, without power-law cross-over, as exemplified by the thermal cascade  $(T+L)_B$  in Fig. 3.

Wideband cascade spectra are obtained by averaging over multiple electron populations,

$$\langle p^{T,L}(\omega) \rangle := \sum_i \langle p^{T,L}(\omega; \gamma_i, n_i) \rangle_{\alpha_i, \beta_i}. \quad (10)$$

Similar linear combinations, including pure power-laws, have been used to model  $\gamma$ -ray burst spectra [20,21] and electron distributions in galaxy clusters [22]. The normalization factors  $A_{\alpha_i, \beta_i}(\gamma_i, n_i)$  of the individual averages in this series are calculated via

$$n_i = A_{\alpha_i, \beta_i}(\gamma_i, n_i) \int_{\gamma_i}^{\infty} d\rho_{\alpha_i, \beta_i}(\gamma), \quad (11)$$

where  $n_i$  is the electron count and  $\gamma_i$  the smallest Lorentz factor in the population defined by  $d\rho_{\alpha_i, \beta_i}$ . The electron numbers  $n_i$  (attached to a power-law index  $\alpha_i$ , temperature  $\beta_i = mc^2/(kT_i)$ , and interval boundary  $\gamma_i$ ) determine the weights in the linear combination (10).

We summarize the flux density plotted in Figs. 1 and 3. The spectral fit is done for unpolarized radiation, so that we start by summing over the polarization components,

$$E^2 \frac{dN}{dE} = E^2 \frac{dN^T}{dE} + E^2 \frac{dN^L}{dE}. \quad (12)$$

We plot the unpolarized  $E^2$ -scaled flux density  $E^2 dN/dE$ , as well as the polarization components  $E^2 dN^{T,L}/dE$ . (We occasionally use a superscript T+L to indicate the total flux density, writing  $dN^{T+L}$  instead of  $dN$ .) The polarization components in (12) are obtained by summing over two cascades, cf. (8) and (10),

$$E^2 \frac{dN^{T,L}}{dE} = \sum_{i=1}^2 E^2 \frac{dN^{T,L}(E; \alpha_i, \beta_i, \gamma_i, n_i)}{dE}. \quad (13)$$

The individual cascades used in the least-squares fit described in the caption of Fig. 2 are assembled from (2), (4), (5) and (8). Restoring dimensions, we find their explicit shape as

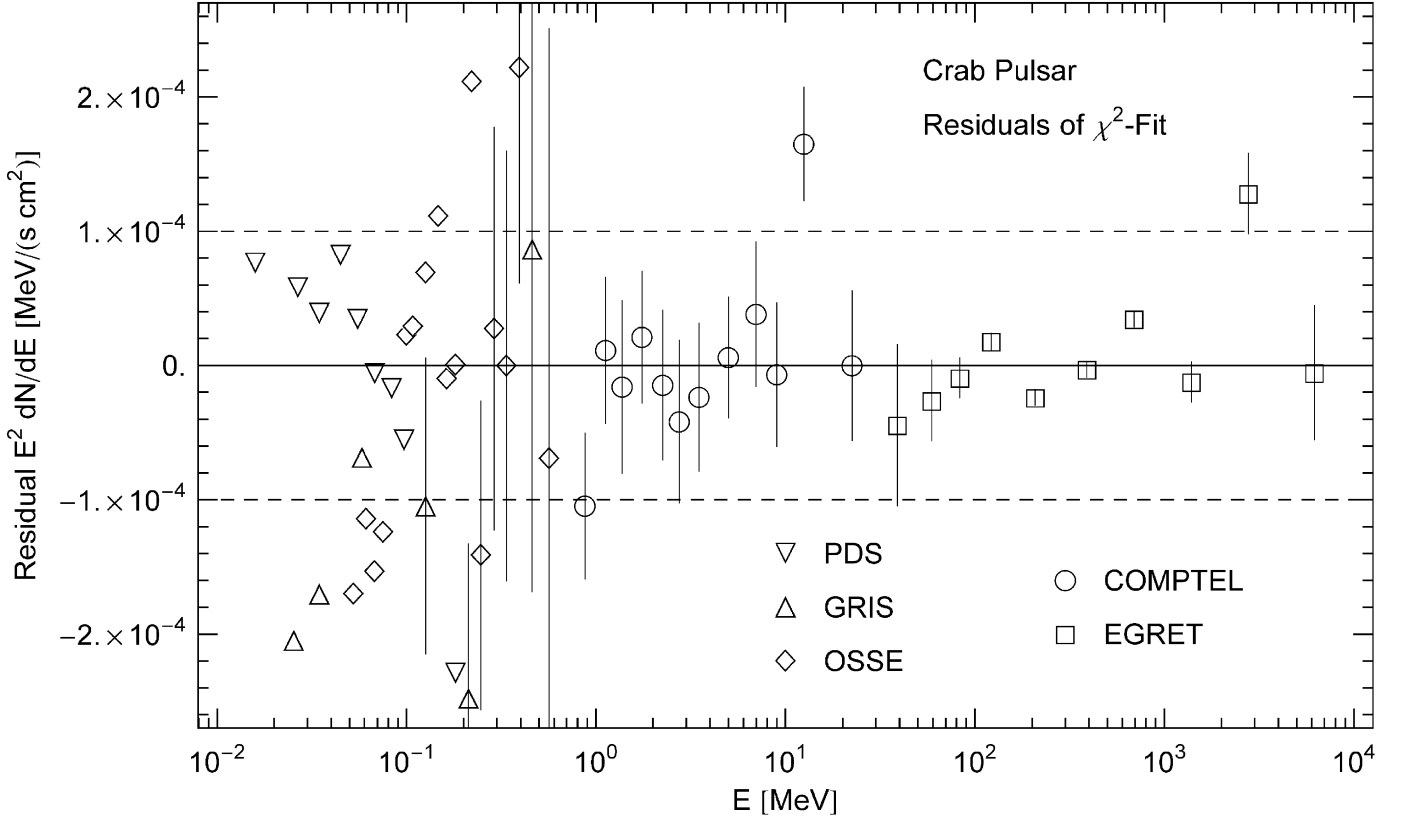


Fig. 2. Residuals of the least-squares fit in Fig. 1. The cascade  $\rho_1$  in Fig. 1 is based on ten EGRET flux points; the ninth point above the  $10^{-4}$ -mark is discounted in the  $\chi^2$ -fit. This cascade is fitted with  $\chi^2 \approx 3.85$  (unreduced) and a confidence level of 57% with 5 dof. The cascade depends nonlinearly on the four fitting parameters, which limits the significance of Gaussian  $p$ -values,  $\Gamma(\text{dof}/2, \chi^2/2)/\Gamma(\text{dof}/2)$ , apart from the low statistics. For instance, the first seven points of the EGRET plateau amount to a horizontal straight-line fit effectively depending on only one independent fitting parameter, which suggests a much higher confidence level. The  $\rho_2$ -cascade in Fig. 1 on top of  $\rho_1$  is based on the COMPTEL points. The first and last of the indicated 12 COMPTEL points are discarded in the fit, and  $\chi^2$  is weighted with the indicated error bars. We find  $\chi^2 \approx 1.40$  and a confidence level of 97% with 6 dof. This high  $p$ -value is mainly due to the larger error bars, as compared to the EGRET fit. The PDS, GRIS and OSSE points are not included in the  $\chi^2$ -fit of the  $\rho_2$ -cascade, but it is evident from the rather symmetrically spaced residuals that the cascade is a good fit to these dispersed data sets. The residuals (data points minus fitting function (12)–(15) with parameters as in Table 1) have not been normalized.

$$\begin{aligned}
 E^2 \frac{dN^{\text{T,L}}(E; \alpha_i, \beta_i, \gamma_i, n_i)}{dE} &= \frac{n_i E}{4\pi d^2 \hbar \int_{\gamma_i}^{\infty} y^{-\alpha_i-1} e^{-\beta_i y} \sqrt{y^2 - 1} dy} \\
 &\times \left( B^{\text{T,L}}(E; \gamma_i; \alpha_i, \beta_i) \theta\left(\sqrt{\gamma_i^2 - 1} - \frac{E}{m_i c^2}\right) \right. \\
 &+ B^{\text{T,L}}\left(E; \sqrt{1 + \frac{E^2}{m_i^2 c^4}}; \alpha_i, \beta_i\right) \\
 &\left. \times \theta\left(\frac{E}{m_i c^2} - \sqrt{\gamma_i^2 - 1}\right) \right). \quad (14)
 \end{aligned}$$

Each cascade depends on four fitting parameters,  $\alpha_i$ ,  $\beta_i$ ,  $\gamma_i$ ,  $n_i$ , whose meaning is explained at the beginning of this section. [The actual spectral fit described in the figure captions is done by at first summing over the polarizations in (14) and by adding the  $\chi^2$ -fits of the unpolarized cascades  $E^2 dN^{\text{T+L}}(E; \alpha_i, \beta_i, \gamma_i, n_i)/dE$ . That is, we interchange the summations in (12) and (13) to obtain  $E^2 dN/dE$ .]  $\theta$  is the Heaviside step function, and we use the shortcut

$$\begin{aligned}
 B^{\text{T,L}}(E; x; \alpha, \beta) &:= \frac{\alpha_q m_i^2 c^4 E}{E^2 + m_i^2 c^4} \frac{1}{x^{\alpha+1} \beta^2} \\
 &\times \left( \left( (1 + \alpha)\alpha - \beta^2 \left(1 + \frac{E^2}{m_i^2 c^4}\right) \right) \Delta^{\text{T,L}} \right) \\
 &\times (\beta x)^{\alpha+1} \Gamma(-\alpha - 1, \beta x) - (\alpha - \beta x) e^{-\beta x}, \quad (15)
 \end{aligned}$$

where we put  $\Delta^{\text{T}} = 1$  and  $\Delta^{\text{L}} = 0$ , for transversal and longitudinal polarization, respectively.

The total tachyonic flux density  $E^2 dN/dE$  is plotted in Figs. 1 and 3 (solid line T + L). The individual unpolarized cascades,  $E^2 dN^{\text{T+L}}(E; \alpha_i, \beta_i, \gamma_i, n_i)/dE$ , obtained by summing over the polarizations in (14), are labeled  $\rho_{i=1,2}$  (dashed curves). They add up to the total tachyonic flux density labeled T + L. The electron densities  $\rho_i$  in Table 1 produce the cascade spectra  $\rho_i$  and are in turn defined by parameters  $(\alpha_i, \beta_i, \gamma_i, \hat{n}_i)$  obtained from the least-squares fit.

The cutoff  $kT$  in the electron energy is listed in Table 1, for each electron population generating a cascade in the  $\gamma$ -ray wideband. In the case of protonic source particles, the

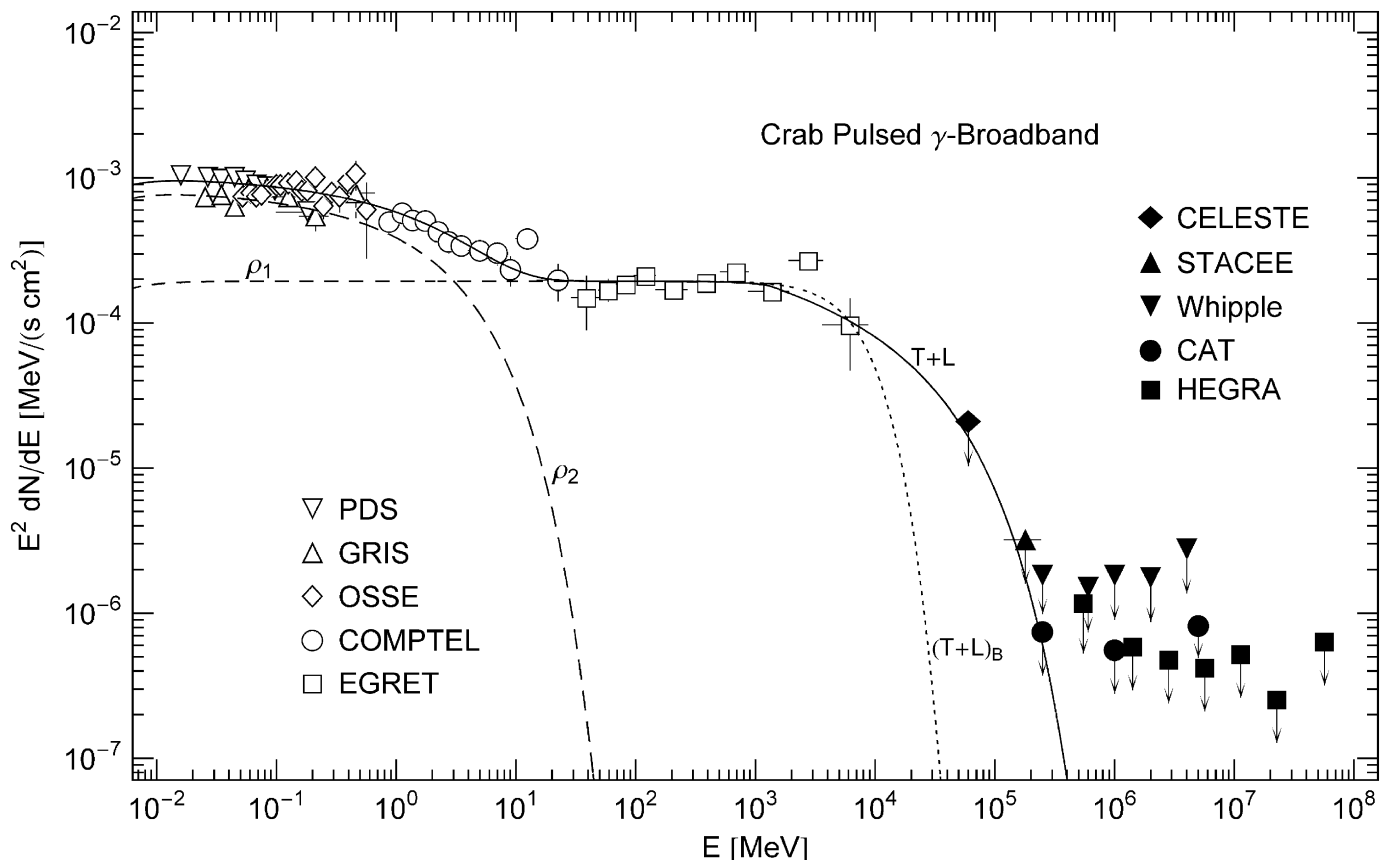


Fig. 3.  $\gamma$ -Ray wideband of the Crab pulsar. Data points depicted as open symbols are referenced in Fig. 1. Filled symbols (upper bounds) from CELESTE [15], STACEE [16], Whipple [17], CAT [18], and HEGRA [19]. The spectral fit T + L (solid line) is done with the rescaled unpolarized tachyon flux  $E^2 dN^{T+L}/dE$  as in Fig. 1. The GeV power-law slope following the spectral break at 1.3 GeV terminates in exponential decay. The GeV-fit hinges on the last EGRET point, the CELESTE and STACEE points, and the first CAT point. The latter three data points are upper limits. Another option for the high-energy fit is the dotted extension (T + L)<sub>B</sub> of the MeV plateau, fitted to the EGRET points only, the upper bounds are evidently satisfied. This fit is based on a thermal Boltzmann distribution generating the  $\rho_1$ -cascade, the parameters of the electron density  $\rho_1$  in Table 1 are replaced by  $\alpha = -2$ ,  $\beta \approx 7.17 \times 10^{-7}$  and  $\gamma = 1$ , and  $\hat{n}$  remains unchanged. In this case, there is no power-law interface between the MeV plateau and exponential decay. Presently, there are not enough data points in the GeV band to discriminate between the exponentially cut power-law fit T + L and the thermal fit (T + L)<sub>B</sub>.

Table 1  
Electronic source densities  $\rho_i$  generating the tachyonic cascade spectra of the Crab pulsar

	$\alpha$	$\beta$	$\gamma$	$\hat{n}$	$n^e$	$kT$ (TeV)
$\rho_1$	1.0	$2.39 \times 10^{-8}$	$6.0 \times 10^5$	$2.1 \times 10^{-2}$	$4.8 \times 10^{48}$	21
$\rho_2$	0.6	$3.31 \times 10^{-4}$	1	$9.0 \times 10^{-2}$	$2.1 \times 10^{49}$	$1.5 \times 10^{-3}$

Each distribution is defined by parameters  $(\alpha, \beta, \gamma, \hat{n})$ , cf. Eq. (2).  $\alpha$  is the electronic power-law index,  $\beta$  the cutoff parameter in the Boltzmann factor, and  $\gamma$  the lower edge of Lorentz factors in the source population.  $\hat{n}$  is the amplitude of the tachyonic flux density generated by  $\rho_i$ . The electron count  $n^e$  is inferred from  $\hat{n}$  via (9) and  $d \approx 2$  kpc.  $kT$  is the electron temperature. The  $\rho_{1,2}$ -cascades in Figs. 1 and 3 are obtained by averaging the superluminal radiation densities (1) with the electron distributions  $\rho_{1,2}$  listed here. The parameters  $(\alpha, \beta, \gamma, \hat{n})$  are extracted from the spectral fit.

cutoff energies have to be multiplied with  $1.8 \times 10^3$ , the proton/electron mass ratio. These cutoffs are to be compared to two spectral breaks in the cosmic-ray spectrum, occurring at  $10^{3.5}$  TeV and  $10^{5.8}$  TeV, dubbed knee and second knee, respectively [23]. A protonic source density generating the  $\rho_1$ -cascade has a cutoff at about  $10^{4.6}$  TeV, suggest-

ing protons in the pulsar magnetosphere with energies between the first and second knee.

#### 4. Conclusion

We have considered superluminal spectral densities generated by freely moving electrons, discussed the spectral averaging with electronic source distributions, and derived the high- and low-temperature expansions of the averaged radiation densities. We demonstrated that the  $\gamma$ -ray flux of the Crab pulsar can be reproduced by tachyonic cascade spectra, and explained the spectral plateau, the power-law slopes, and the spectral curvature.

Here, we have studied superluminal radiation from electrons in uniform motion. Tachyonic synchrotron and cyclotron radiation was investigated in [24,25]. In the zero magnetic field limit, the tachyonic synchrotron densities converge to the spectral densities (1) for uniform motion. Electromagnetic synchrotron radiation vanishes in this limit, of course. A finite bending radius induces

modulations in the spectral densities. These oscillations are quite small, just tiny ripples along the spectral slope with increasing amplitude toward the spectral break [25]. If integrated over a thermal or power-law electron distribution as done here, these oscillations are averaged out.

Several electromagnetic radiation mechanisms have been invoked to model the spectra of  $\gamma$ -ray pulsars, most notably curvature radiation due to electric fields followed by pair creation, accompanied by synchrotron radiation and inverse Compton scattering [26]. These mechanisms are quite interlocked, cf. the flow-chart in [27], and subject to frequent revisions [28,29]. An electromagnetic spectral fit to the pulsed Crab emission, directly comparable to Fig. 1, can be found in Fig. 11 of [28].

In Section 3, we pointed out that only a fraction  $\alpha_q/\alpha_e \approx 1.4 \times 10^{-11}$  of the tachyon flux arriving at the detector is actually absorbed, so that the measured flux has to be rescaled with the ratio of electric and tachyonic fine structure constant. This rescaling applies to  $\gamma$ -ray spectra only, to frequencies much higher than the 2 keV tachyon mass, so that the mass-square can be dropped in the tachyonic dispersion relation. At X-ray energies, we have to rescale with the respective cross-section ratio,  $\sigma_e(\omega)/\sigma_q(\omega)$ , where  $\sigma_e$  is the electromagnetic cross-section and  $\sigma_q$  its tachyonic counterpart. The detection mechanism for hard and high-energy X-rays is usually ionization, generating scintillations in NaI(Tl) and CsI(Na) crystals of phoswich detectors [30], or gas scintillations by ionization of Xenon atoms in proportional counters [31]. Tachyonic ionization cross-sections of hydrogen-like ground states, that can be used for X- as well as  $\gamma$ -rays, have been calculated in [32]. At  $\gamma$ -ray energies, photonic and tachyonic dispersion relation coincide, and the cross-section ratio of the detection mechanism (such as ionization [33], Compton scattering [34] and pair production [35], the latter two quantified by Klein-Nishina and Bethe–Heitler cross-section) approaches a constant limit value  $\alpha_e/\alpha_q$ , which amounts to an overall rescaling of the tachyonic flux amplitude. By contrast, at X-ray energies, we would have to rescale the tachyonic flux density with the energy dependent cross-section ratio, which affects the shape of the spectral map. If a grating spectrometer is used, the interference peaks are determined by wavelength. In this case, the observational plots have to be reparametrized by wavelength, and then the tachyonic dispersion relation is substituted to obtain the actual energy-flux relation.

## Acknowledgement

The author acknowledges the support of the Japan Society for the Promotion of Science. The hospitality and stimulating atmosphere of the Centre for Nonlinear Dynamics, Bharathidasan University, Trichy, and the Institute of Mathematical Sciences, Chennai, are likewise gratefully acknowledged.

## References

- [1] J.A. Wheeler, R.P. Feynman, *Rev. Mod. Phys.* 17 (1945) 157.
- [2] R. Tomaschitz, *Class. Quantum Grav.* 18 (2001) 4395.
- [3] R. Tomaschitz, *Physica A* 320 (2003) 329.
- [4] R. Tomaschitz, *Eur. Phys. J. B* 17 (2000) 523.
- [5] W. Magnus, F. Oberhettinger, R.P. Soni, *Formulas and Theorems for the Special Functions of Mathematical Physics*, Springer, New York, 1966.
- [6] R. Tomaschitz, *Astropart. Phys.* 23 (2005) 117.
- [7] L. Kuiper et al., *Astron. Astrophys.* 378 (2001) 918.
- [8] L.M. Bartlett et al., *AIP Conf. Proc.* 304 (1994) 67.
- [9] M.P. Ulmer et al., *Astrophys. J.* 432 (1994) 228.
- [10] R. Much et al., *Astron. Astrophys.* 299 (1995) 435.
- [11] R. Much et al., *Astron. Astrophys. Suppl. Ser.* 120 (1996) 703.
- [12] R.D. van der Meulen et al., *Astron. Astrophys.* 330 (1998) 321.
- [13] R.C. Hartman et al., *Astrophys. J. Suppl.* 123 (1999) 79.
- [14] J.M. Fierro et al., *Astrophys. J.* 494 (1998) 734.
- [15] M. de Naurois et al., *Astrophys. J.* 566 (2002) 343.
- [16] S. Oser et al., *Astrophys. J.* 547 (2001) 949.
- [17] R.W. Lessard et al., *Astrophys. J.* 531 (2000) 942.
- [18] A. Musquère et al., in: D. Kieda, M. Salamon, B. Dingus (Eds.), *Proceedings of the 26th International Cosmic Ray Conference*, Salt Lake City, 1999, vol. 3, p. 460.
- [19] F. Aharonian et al., *Astrophys. J.* 614 (2004) 897.
- [20] D. Band et al., *Astrophys. J.* 413 (1993) 281.
- [21] N.M. Lloyd, V. Petrosian, *Astrophys. J.* 511 (1999) 550.
- [22] V. Petrosian, *Astrophys. J.* 557 (2001) 560.
- [23] M. Nagano, A.A. Watson, *Rev. Mod. Phys.* 72 (2000) 689.
- [24] R. Tomaschitz, *Physica A* 335 (2004) 577.
- [25] R. Tomaschitz, *Eur. Phys. J. C* 45 (2006) 493.
- [26] K.S. Cheng, C. Ho, M. Ruderman, *Astrophys. J.* 300 (1986) 500.
- [27] C. Ho, *Astrophys. J.* 342 (1989) 396.
- [28] K.S. Cheng, M. Ruderman, L. Zhang, *Astrophys. J.* 537 (2000) 964.
- [29] J. Takata et al., *Mon. Not. R. Astron. Soc.* 366 (2006) 1310.
- [30] F. Frontera et al., *Astron. Astrophys. Suppl. Ser.* 122 (1997) 357.
- [31] G. Manzo et al., *Astron. Astrophys. Suppl. Ser.* 122 (1997) 341.
- [32] R. Tomaschitz, *Eur. Phys. J. D* 32 (2005) 241.
- [33] W.N. Johnson et al., *Astrophys. J. Suppl.* 86 (1993) 693.
- [34] V. Schönfelder et al., *Astrophys. J. Suppl.* 86 (1993) 657.
- [35] D.J. Thompson et al., *Astrophys. J. Suppl.* 86 (1993) 629.